

Numerical investigation of noise generation by rod-airfoil configuration using DES (SU2) and the FW-H analogy

Sparsh Sharma* and Thomas Geyer†

Brandenburg Technical University Cottbus-Senftenberg, 03046 Cottbus, Germany

Ennes Sarradj‡

Technical University Berlin, 10587 Berlin, Germany

Heiko Schmidt§

Brandenburg Technical University Cottbus-Senftenberg, 03046 Cottbus, Germany

The generation of broadband noise in turbomachinery is influenced by the effects of unsteady loading. This paper aims at predicting that noise by numerically simulating the classical case of an airfoil embedded in the wake of a circular cylinder using the Detached-Eddy Simulation (DES) suite of the SU2 solver coupled with the Ffowcs-Williams and Hawkins (FW-H) technique. The rod-airfoil configuration is numerically simulated to study the noise generation dependency on cylinder size (diameter) and the gap between the cylinder and the leading edge of the airfoil. A detailed experimental study and numerical simulations available enable the validation of the approach. The main aim of the study is to investigate (i) the impact of geometric effects (cylinder diameter and the gap between the cylinder and airfoil) on the noise generation, and (ii) the applicability of the SU2 solver in aeroacoustics. Even for 2D simulations, it was found that the parameters of the turbulent wake of the cylinder were reproduced sufficiently well. Regarding the generated noise, however, the current study shows that a 2D simulation only enables the prediction of very basic trends. A better prediction of the impact of the geometric effects on the noise generation, as observed in accompanying wind tunnel experiments, possibly require a 3D simulation and hence a notably increased computational effort.

Nomenclature

b	= span width [m]
c	= speed of sound [m/s]
c_l	= lift coefficient
d	= cylinder diameter [m]
f	= frequency [1/s]
f_c	= (third-octave band) center frequency [1/s]
g	= gap width [m]
L_p	= sound pressure level [dB]
M	= Mach number
Re_d	= Reynolds number (based on cylinder diameter)
s	= chord length [m]
Sr	= Strouhal number
U_∞	= inflow velocity [m/s]
\overline{U}	= mean velocity [m/s]

*Doctoral Researcher, Technical Acoustics, Brandenburg Technical University Cottbus-Senftenberg.

†Academic Researcher, Technical Acoustics, Brandenburg Technical University Cottbus-Senftenberg.

‡Professor, Technical Acoustics, Technical University Berlin, Berlin.

§Professor, Numerical Fluid and Gas Dynamics, Brandenburg Technical University Cottbus-Senftenberg.

u'	=	rms velocity [m/s]
CAA	=	Computational Aeroacoustics
CFD	=	Computational Fluid Dynamics
DES	=	Detached Eddy Simulation
DDES	=	Delayed Detached Eddy Simulation
DNS	=	Direct Numerical Simulation
FFT	=	Fast Fourier Transformation
LE	=	leading edge
LES	=	Large Eddy Simulation
PDE	=	Partial Differential Equations
SGS	=	Subgrid Scale
TE	=	trailing edge
RANS	=	Reynolds Averaged Navier-Stokes

I. Introduction

ACOUSTIC radiation from an airfoil subjected to a real flow is comprised of two parts: The first is trailing edge noise due to the interaction of the airfoil boundary layer with the trailing edge, and the second is leading edge noise which is due to the interaction of the leading edge with oncoming flow disturbances. At reasonable angles of attack and highly perturbed flow, the latter one becomes dominant in terms of unsteady loading and the resulting acoustic radiation [1]. This is an important broadband noise generating mechanism and can be observed in many practical assemblies, e.g. fans and compressors in aircraft engines, rotor-stator-configurations in air-conditioning units and fans placed behind a heat exchanger.

In order to predict the sound radiation from the airfoil, apart from wind tunnel experiments, Computational Aeroacoustics (CAA) provides a highly capable path to better understand the flow physics and to speed up the design process. CAA has attracted much attention in recent times because of its obvious requirement in practical applications. Many researchers [2, 3] used a cylinder placed upstream to create a turbulent wake (a *von Kármán* street of counter-rotating vortices at a nearly constant Strouhal number $Sr = f \cdot d / U_\infty \approx 0.2$, where f is the shedding frequency, d the cylinder diameter and U_∞ the flow velocity). This wake then interacted with another cylinder or airfoil downstream. The studies were mainly focused on the flow features in the interaction region such as the vortex shedding and flow patterns.

This so-called rod-airfoil configuration has been extensively studied numerically under various approaches, for example *Unsteady Reynolds Averaged Navier-Stokes* (URANS) [3, 4] and *Large Eddy Simulations* (LES) [5–8]. In these papers, reliable results are not obtained using URANS. Jiang et al. [9] observed substantial differences between the numerical noise spectra and the experimental one. This behaviour may be attributed to the fact that it is difficult for RANS to resolve the strong unsteady phenomena consequential from the impingement of the turbulent wake on the airfoil, which is mainly responsible for the noise radiation. Indeed only *Direct Numerical Simulation* (DNS) would be able to simulate the flow around the cylinder, in the gap, and along the airfoil without the need of any turbulence model. Since the computational effort of DNS scales in three dimensions with Re^4 , where Re is the Reynolds number, the ansatz will not be applicable for realistic airfoil simulations in the foreseeable future. LES lies in between RANS and DNS, although for high Re number flows realistically it is closer to RANS since only the very large scales can be simulated, while all the rest is still modeled. The LES method requires more grid resolution and corresponding small time steps to resolve the small turbulent scales than RANS, thus requiring a higher computational cost. Additionally, LES does not perform well at rigid boundaries. Another class of numerical techniques is called *Detached Eddy Simulation* (DES), a hybrid model that functions like RANS in the near-wall regions and like LES in detached flow zones, and hence combines advantages of both methods while being less demanding than pure LES [10]. DES solutions are expected to approach the quality of an LES prediction with optimised computational cost and are hence an excellent option for simulating the rod-cylinder case. Greschner et al. [11] used the DES approach to simulate the rod-airfoil configuration and indicated the effectiveness of the method in terms of computational cost and accuracy in the prediction of flow over blunt bodies. Zhou et al. [12] used a rod-airfoil configuration in a *Delayed Detached Eddy Simulation* (DDES) with the aim to optimize the shape of a NACA 0012 airfoil regarding a minimum turbulence interaction noise. Table 1

summarizes the recent numerical work on rod-airfoil configurations using DES, DDES and LES.

The above discussion shows that the studies in the past have mainly been focusing on the flow physics of the interaction of the turbulent wake, generated by the rod, with the airfoil. The main aim of the present study is to investigate (i) the impact of geometric effects (cylinder diameter and the gap between the cylinder and airfoil) on the noise generation due to the unsteady loading on an airfoil placed downstream of a circular cylinder, and (ii) the applicability of the open source solver *Stanford University Unstructured* (SU2) for aeroacoustic problems. Thereby, SU2 is used to obtain the unsteady aerodynamic solution for the case, which is then used as the input for the Ffowcs Williams-Hawkings (FWH) equation [13] to obtain the aeroacoustic results. The so numerically obtained sound pressure level spectra are validated against available experimental spectra [14, 15].

Table 1 Numerical studies

Name	Year	Method	Mesh
Zhou et al. [12]	2017	DDES	3D Unstructured
Jiang et al. [8]	2015	LES	3D Structured
Agrawal and Sharma [7]	2014	LES	3D Unstructured
Giret et al. [6]	2012	LES	3D Unstructured
Galdeano et al. [16]	2010	DES	3D Unstructured
Berland et al. [5]	2010	LES	3D Structured
Greschner et al. [17]	2008	DES	3D Structured
Caraeni et al. [18]	2007	DES	3D Unstructured
Gerolymos and Vallet [19]	2007	DES	3D Structured
Greschner et al. [11]	2004	DES	3D Unstructured

II. Numerical Setup

A. Method

The rod-airfoil configuration is investigated numerically using SU2 [20], an open source suite written in C++ and Python to numerically solve partial differential equations (PDE). Using this solver, Molina et al. [21, 22] have successfully demonstrated the capabilities of DES in aeroacoustic applications. The numerical results were obtained for a tandem cylinder case using the Delayed Detached Eddy Simulation. Zhou et al. [12] used the same approach for the rod-airfoil configuration.

Molina et al. [22] briefly reviewed the hybrid RANS/LES methods and divided them into two broad categories: Non-zonal* and zonal[†] hybrid approaches. For the present work, a non-zonal hybrid approach, DDES which uses shear-layer adaptive subgrid scale (SGS), is used to investigate the feasibility of hybrid models based on a two-dimensional setup. In the DDES method, a function is introduced that detects boundary layers and extends the full RANS mode, postponing the switch into the LES mode based on the local flow solution. In total, eight different cases (explained in the next section) of the rod-airfoil configuration were simulated using the DDES approach to obtain the unsteady aerodynamic solution.

In the present study, numerical results obtained only for a two-dimensional mesh will be shown. Naturally, this is a simplification, since turbulence generated by a real cylinder in a flow is, of course, a three-dimensional phenomenon. For one, in a 2D simulation, the flow does not have a third dimension to go to, so the levels of fluctuation tend to be stronger compared to a 3D simulation and measurements. Hence, the present analysis rather focuses on the question of whether trends regarding variations of the parameters of the configuration, as observed in the experiments, can be reproduced by the simulations at least to some extent.

*the model, not the user, defines the regions where RANS and LES modes are active

[†]the user specifies the RANS to LES transition region through a synthetic turbulence interface

B. Configuration Description

The schematic diagram of the configuration to be investigated is shown in Fig. 1. It consists of an airfoil embedded in the wake of a circular rod. The wake is characterized as the classical von Kármán vortex shedding from the cylinder and can be regarded as an oncoming disturbance onto the airfoil. The importance of studying the rod-airfoil configuration is well documented in an extensive review published by Zdravkovich [2]. This problem was first investigated experimentally by Jacob et al. [4] with a prime motive to build an experimental database against which state-of-the-art CAA/CFD techniques could be tested. Vortices shed from the rod convect downstream and impinge on the airfoil. This interaction yields unsteady lift on the airfoil, which is radiated as noise. Tones with broadened peaks above the broadband noise background are observed at the shedding frequency [4].

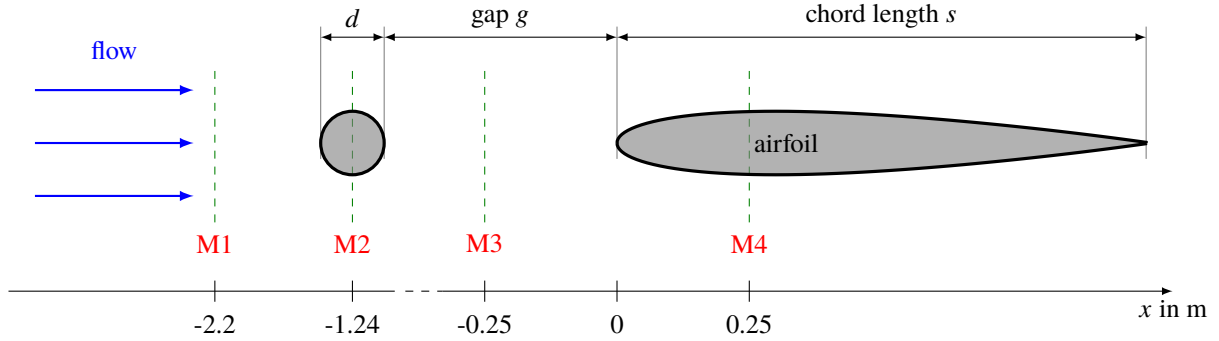


Fig. 1 Schematic of the rod-airfoil configuration (side view, the dashed lines denote locations at which velocity profiles were extracted; not to scale)

In corresponding experiments by Giesler [14, 15], the flow speed was adjusted between 26 m/s and 72 m/s in 27 steps, and two airfoils of NACA 0012 shape and one of NACA 0018 shape with a chord length s of 100 mm and a span width b of 120 mm were used. The turbulence was generated by rods with 5 mm, 7 mm, 10 mm, 13 mm and 16 mm diameter and a length of 120 mm. The gap was adjusted to 86 mm, 96 mm, 106 mm, 113 mm and 124 mm. A total of 75 configurations have been tested. In the present paper, the rod diameter, d , and the gap between the rod and the airfoil, g , is varied. Fig. 2(a) shows the two-dimensional computational domain for the configuration, which extends 20 chord lengths s upstream of the cylinder, 20 s downstream of the airfoil, and 10 s to each side of the cylinder. The boundary at the left side was set as velocity inlet and on the right side as pressure outlet, the remaining upper and lower boundaries were set as ambient walls. The mesh was refined near the cylinder and airfoil wall, as shown in Fig. 2(b). The airfoil is set at angle of attack of zero degrees in the simulations as was done in the experiments. A fully unstructured grid was generated using the Pointwise mesh generation software. A C-type grid was used around the airfoil and an O-type grid around the cylinder to resolve the boundary layers on the bodies. The aspect ratio of the mesh elements between the rod and airfoil is approximately unity with a nearly constant grid spacing. The grid is coarsened in the outer block to reduce the computational cost. It is composed of about 4 million cells with 300 points around the rod and 400 points around the NACA 0012 in the circumferential direction. The normalized first cell spacing normal to the wall is $y^+ < 1.0$.

The two-dimensional configuration was simulated for two velocities corresponding to the minimum, 26 m/s, and the maximum, 72 m/s, of the experimental setup used by Giesler [14, 15]. Only the NACA 0012 airfoil with a chord length s of 100 mm was used. To achieve the variation in the incoming disturbance, the diameter of the cylinder and the gap between the center of the cylinder and the airfoil leading edge (LE) were varied. Cylinders were sized as $d = 5$ mm and 16 mm and the gap was adjusted as $g = 86$ mm and 124 mm. All the cases are listed in Table 2. The time step in the simulations was set to be $\Delta t = 1 \times 10^{-5}$ s, with a total simulation time of 0.1 s (corresponding to 10,000 iterations). All simulations were conducted on a 16 core Intel i7-8700K workstation.

III. Experimental Setup

Corresponding measurements were conducted in the small aeroacoustic open jet wind tunnel at the Brandenburg University of Technology Cottbus - Senftenberg [23], using cylinders of identical diameters and a NACA 0012

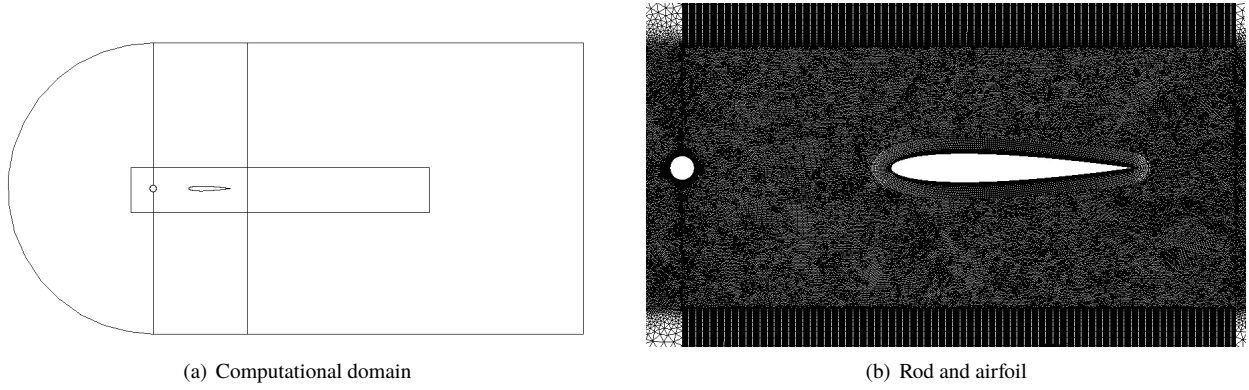


Fig. 2 Computational domain and mesh used for the numerical calculations

Table 2 Overview of test cases for numerical studies

case	cylinder diameter d (mm)	gap g (mm)	flow velocity (m/s)	airfoil type
1	5	86	26	NACA 0012
2	5	86	72	NACA 0012
3	5	124	26	NACA 0012
4	5	124	72	NACA 0012
5	16	86	26	NACA 0012
6	16	86	72	NACA 0012
7	16	124	26	NACA 0012
8	16	124	72	NACA 0012

airfoil of the same chord length. The nozzle used in the experiments has a rectangular exit area with dimensions of $120 \text{ mm} \times 147 \text{ mm}$. Both the cylinder and the airfoil model were mounted between side walls, which were covered with an absorbing foam with a thickness of 50 mm in order to reduce noise from the wall junction. A detailed description of the setup is given in [14, 15].

The acoustic measurements were performed with a planar microphone array, consisting of 38 1/4th inch electret microphone capsules flush-mounted into an aluminium plate with dimensions of $1.5 \text{ m} \times 1.5 \text{ m}$. It was positioned out of the flow, approximately 0.72 m above the airfoil. The data were recorded with a sampling frequency of 51.2 kHz and a duration of 40 s using a 24 Bit National Instruments multichannel frontend. In post-processing, which was done using the open source software package *Acoular* [24], the data was transferred to the frequency domain by a Fast Fourier Transformation (FFT) on blocks of 4,096 samples, using a Hanning window and an overlap of 50 %. The resulting spectra were then averaged to yield the cross-spectral matrix and further processed using the DAMAS beamforming algorithm [25]. This algorithm, although computationally expensive, is known for its good performance especially at low frequencies [26] and is often used in aeroacoustic studies [27]. In the present case, DAMAS was applied to a two-dimensional focus plane parallel to the array. The plane has an extent of 0.65 m in the streamwise direction and 0.4 m in the spanwise direction. With a high resolution of 0.005 m, this leads to a total of 10,611 grid points. In order to obtain quantitative spectra of the noise generated by the airfoil interacting with the inflow turbulence, an integration sector was defined that contains only the noise contributions due to the interaction of the cylinder-generated turbulence with the airfoil. Background noise sources, such as the cylinder itself, but also the interaction of the boundary layer along the side walls with the airfoil, were excluded from the integration. Sources due to the interaction of the turbulent boundary layer with the airfoil trailing edge, however, were included. Finally, the results were converted to sound pressure level spectra *re* 20 μPa .

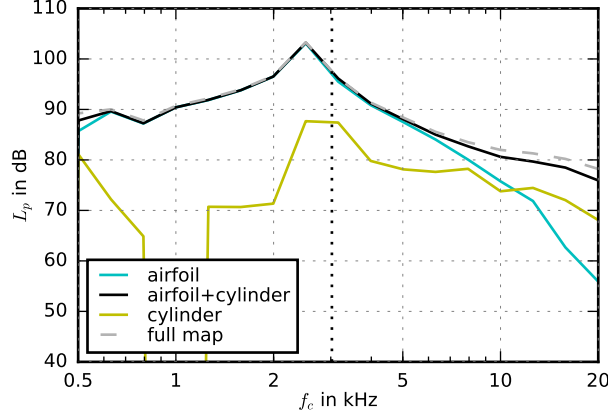


Fig. 3 Comparison of the experimental results for case 2 ($d = 5$ mm, $g = 86$ mm, $U_\infty = 72$ m/s) using different integration sectors (the dotted vertical line denotes the vortex shedding frequency of the cylinder, calculated using a Strouhal number of 0.21 [28])

To highlight the influence of the integration sector, Fig. 3 shows a comparison of the results for different integration sectors for case 2 ($d = 5$ mm, $g = 86$ mm, $U_\infty = 72$ m/s) from Table 2. The integration sectors are (1) the chosen one that contains only the center part of the airfoil, (2) a sector that contains the center parts of both the cylinder and the airfoil, (3) a sector that contains only the center part of the cylinder and (4) a sector that covers the complete beamforming map. Thus, the last sector contains all physical noise sources, including the wind tunnel nozzle as well as the interaction of the wall boundary layer flow with the cylinder and the airfoil. It is visible that the noise generated by the airfoil dominates the total noise at low and medium frequencies. The noise generated by the cylinder, which shows a broad maximum at third-octave band center frequencies of 2.5 kHz and 3.15 kHz, is well below the noise generated by the airfoil. However, it is also visible that the noise generated by the airfoil contains a notable tonal component, which can be assumed to be due to the von Kármán vortices hitting the leading edge.

IV. Numerical Aerodynamic Results

A. Flow Features

In the first step, the fully developed two-dimensional flow is analyzed qualitatively. Fig. 4 shows the resulting vortex shedding as periodic oscillations in the wake of the rods. Thus, a regular Kármán vortex street can be observed in all the cases, since there is no spanwise effect which may prevent the formation of a regular pattern [2]. The non-dimensional shedding frequency for the DDES model corresponds to a value of $St = 0.23 \pm 0.2$, which is slightly larger than the value of 0.21 reported in the literature for this Reynolds number range [28]. A possible explanation for this mismatch was given by Greschner et al. [11], who state that the position of the separation point is not accurately predicted. This leads to an overpredicted shedding frequency. Fig. 5 shows corresponding frequency spectra of the fluctuating lift coefficient c_l of the cylinder at four different Reynolds numbers Re_d (based on cylinder diameter).

Fig. 6 shows the developing flow around case 2 at different instants in the simulation. The vortex shedding plot shows the vortices shed from the rod, which are convected downstream as incoming turbulence to the airfoil. The turbulent wake leads to a wide range of turbulent structures. The larger turbulent structures break down while impinging on the leading edge, whereas the smaller eddies go along the airfoil sides and undergo a distortion.

B. Velocity Profile Comparisons

In order to enable comparisons of the mean and r.m.s. velocity profiles with results reported in [7], simulations were performed on an additional case ($d = 10$ mm, $g = 100$ mm, $s = 100$ mm, $M = 0.2$, NACA 0012) and the data was sampled for 4 periods of wake shedding for the numerical simulation. To this end, the profiles were extracted at five



(a) Case 1 ($d = 5 \text{ mm}$, $g = 86 \text{ mm}$, $U_\infty = 26 \text{ m/s}$)



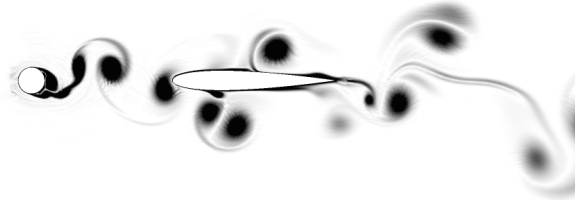
(b) Case 2 ($d = 5 \text{ mm}$, $g = 86 \text{ mm}$, $U_\infty = 72 \text{ m/s}$)



(c) Case 3 ($d = 5 \text{ mm}$, $g = 124 \text{ mm}$, $U_\infty = 26 \text{ m/s}$)



(d) Case 4 ($d = 5 \text{ mm}$, $g = 124 \text{ mm}$, $U_\infty = 72 \text{ m/s}$)



(e) Case 5 ($d = 16 \text{ mm}$, $g = 86 \text{ mm}$, $U_\infty = 26 \text{ m/s}$)



(f) Case 6 ($d = 16 \text{ mm}$, $g = 86 \text{ mm}$, $U_\infty = 72 \text{ m/s}$)



(g) Case 7 ($d = 16 \text{ mm}$, $g = 124 \text{ mm}$, $U_\infty = 26 \text{ m/s}$)



(h) Case 8 ($d = 16 \text{ mm}$, $g = 124 \text{ mm}$, $U_\infty = 72 \text{ m/s}$)

Fig. 4 Vortex shedding at the end of the iterations for all cases (shown is the magnitude of the vorticity $|\vec{\omega}|$)

different streamwise locations, which are marked in Fig. 1.

First, the mean and fluctuating velocities in the streamwise direction are compared with the experimental work. Figs. 7(a) and 7(b) show the mean and the fluctuating velocity extracted at the M1 marker at $x/s = -2.2$, which is upstream of the rod. It is visible that the velocities, essentially the freestream conditions, are well predicted by the DDES.

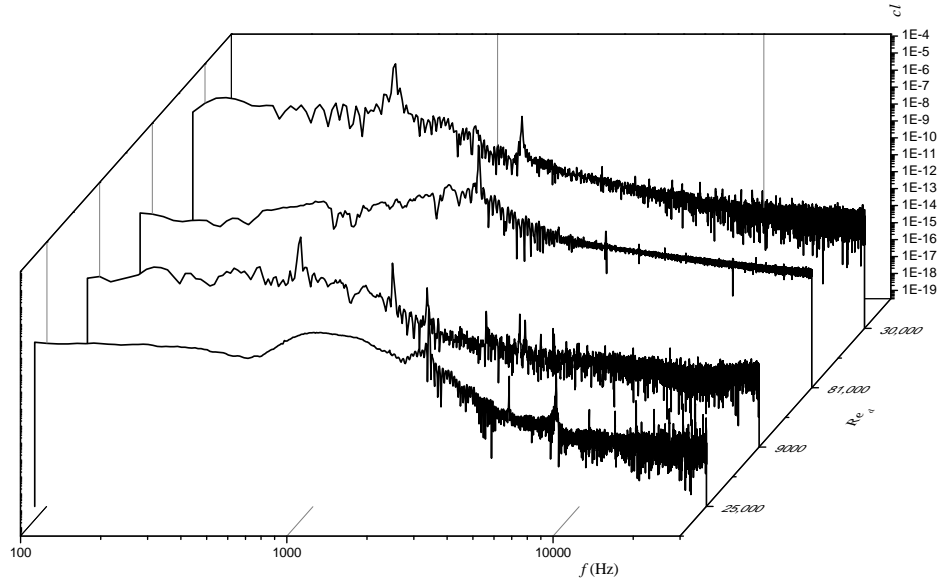


Fig. 5 Spectral analysis of the lift coefficient c_l of the cylinder at four different Reynolds numbers (based on cylinder diameter)

Figs. 7(c) and 7(d) then show the velocity profiles at M2 ($x/s = -1.24$), which bisects the cylinder into equal segments. Again, the profiles obtained from the simulations are in good agreement with the experiments. Figs. 8(a) through 8(d) depict the velocity profiles at M3 (at $x/s = -0.25$) and M4 (at $x/s = 0.25$). The mean velocity at M3 (upstream of the airfoil) is slightly overpredicted, whereas the rms-values of the fluctuating velocity at this location are in good agreement with the experimental data. Basically, this shows that the DDES results agree well with the experimental data except in the near-wall region, as stated earlier by Greschner et al. [11]. The rod wake turbulence due to its high intensity and length scale determines the velocity profiles on the airfoil rather than the boundary layer development.

V. Aeroacoustics Results

This section assesses the data obtained from the CFD solver and the post-processed results from the FW-H solver. The acoustic results are compared with the experimental ones.

A. Radiated acoustic field

The sound pressure was calculated for different observer positions at a distance of 0.72 m from the airfoil using the Ffowcs Williams and Hawkins (FW-H) integration method [13] to the rigid wall surfaces as the integration surfaces. This was done for the complete simulation time of 0.1 s. The FW-H surface integrals were computed with both the circular rod and the airfoil as the sound sources. In agreement with the analysis of the experimental results, however, only the sources attributed to the airfoil are considered here. Thereby, in agreement with [14, 15] the focus of the analysis is on the high-frequency part of the spectrum with frequencies greater than the vortex shedding frequency.

As a first overview of the computational results, Fig. 9 shows narrowband spectra of the sound pressure levels for all eight cases from Table 2. At the lower flow speed (Fig. 9(a)), it is visible that the peak of the sound pressure level for the cases with the 5 mm cylinder is around 500 Hz (for the case with the smaller gap of 86 mm, several local peaks are also visible at multiples of this frequency). The case with the cylinder with a diameter of 16 mm shows a maximum at a lower frequency around 360 Hz for the small gap of 86 mm and a maximum around 500 Hz for the large gap of 124 mm.

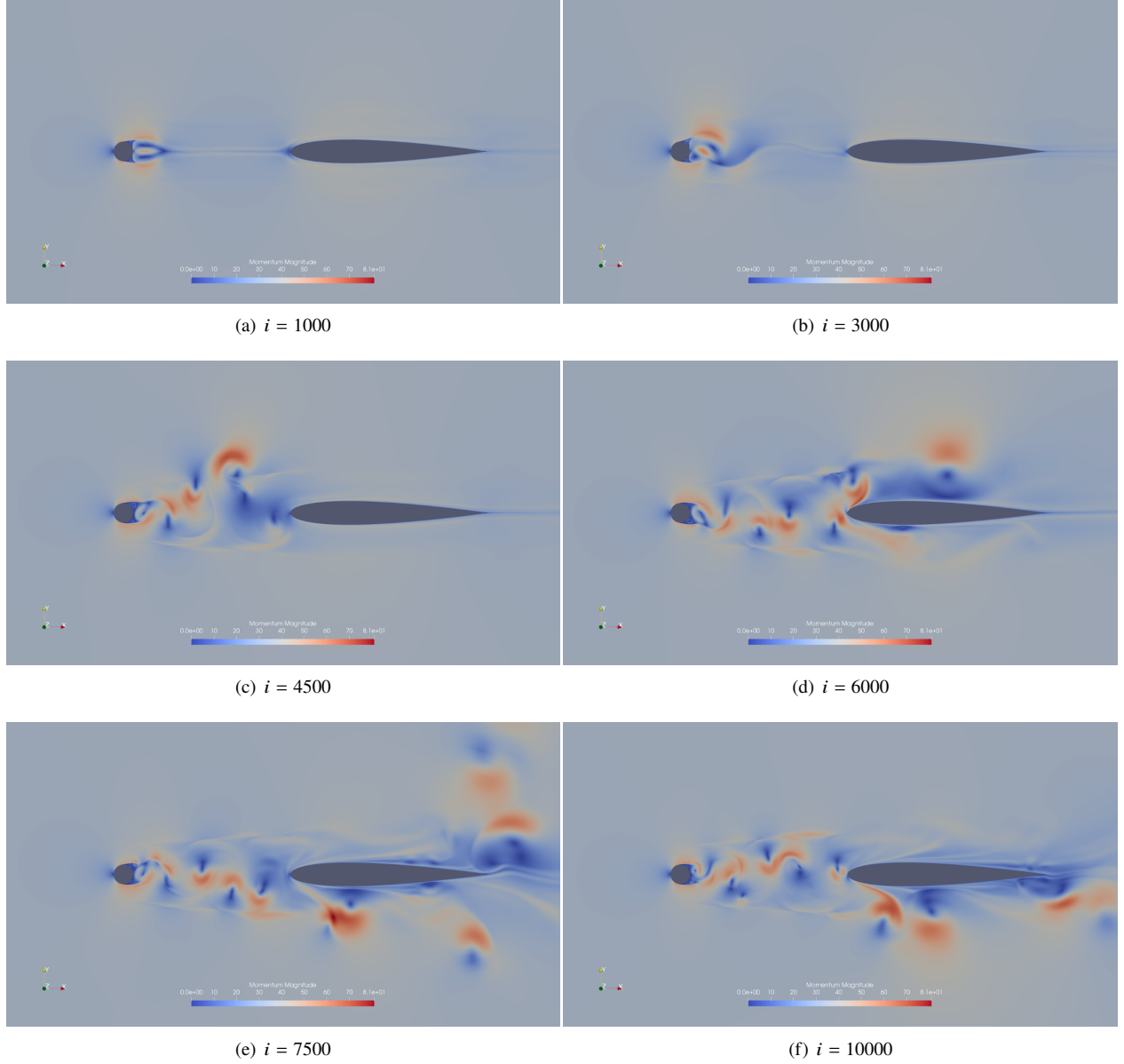
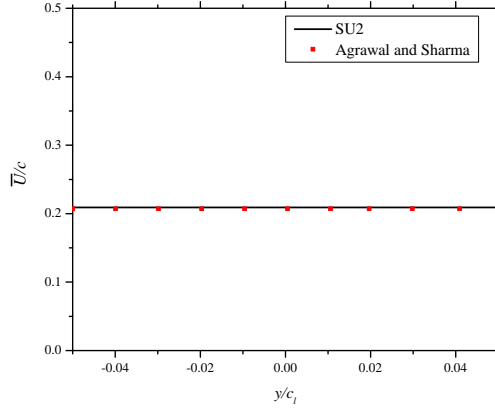
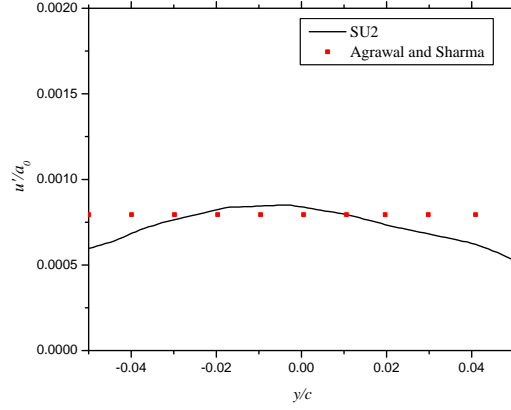


Fig. 6 Vortex shedding at different instants i for case 2 ($d = 16$ mm, $g = 86$ mm, $U_\infty = 26$ m/s; shown is the magnitude of the vorticity $|\vec{\omega}|$)

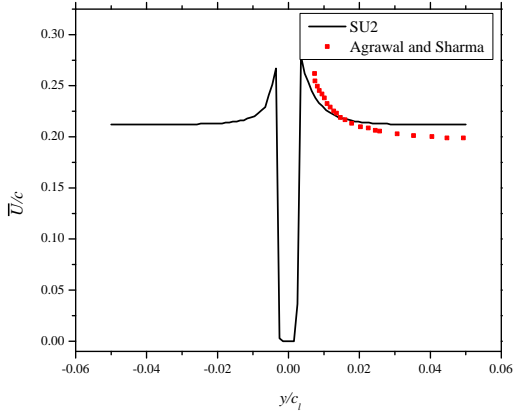
Regarding the overall level, the highest amplitudes at low and medium frequencies were calculated for the case with the thin cylinder and the small gap (case 1), while the lowest noise generation can be observed for the case with the thin cylinder and the large gap (case 3). At the higher flow speed of $U_\infty = 72$ m/s (Fig. 9(b)), an interesting effect can be seen, as each of the configurations leads to a strong maximum at a different frequency. The lowest peak frequency of about 1.1 kHz is seen for case 6 ($d = 16$ mm, $g = 86$ mm), with additional maxima at multiples of this frequency. Considering the respective peak frequency of that configuration at the lower flow speed (360 Hz at 26 m/s) and the ratio of the two flow speeds, this is a somewhat expected result. The peak frequency of the configuration with the thick cylinder and the large gap (case 8) appears around a frequency of 1.7 kHz with additional harmonics, which is larger than the value that would be expected based on the result at the lower flow speed. For case 2 ($d = 5$ mm, $g = 86$ mm), a notable narrowband



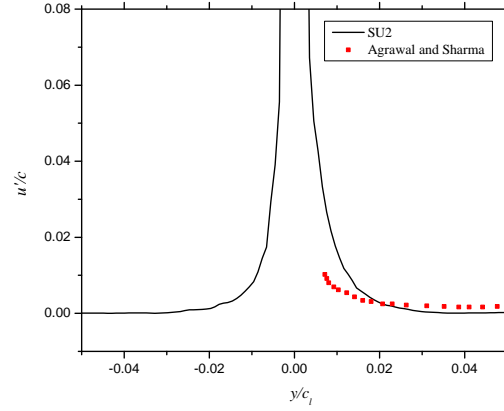
(a) \bar{U}/c at $x/c_l = -2.2$ (M1)



(b) u'/c at $x/c_l = -2.2$ (M1)



(c) \bar{U}/c at $x/c_l = -1.24$ (M2)



(d) u'/c at $x/c_l = -1.24$ (M2)

Fig. 7 Comparison of velocity profiles obtained at markers M1 and M2 (see Fig. 1) from the simulations with experimental data from [7]

spectral maximum can be seen at approximately 2.7 kHz, which also seems unrelated to the result obtained at the lower flow speed. In addition, at frequencies below that strong peak, a broad hump can be seen, whose maximum appears around 1.2 kHz. However, this hump does also seem unrelated to the tonal peak found at the spectra obtained for the lower flow speed. Finally, the sound pressure level spectrum calculated for case 4 ($d = 5$ mm, $g = 124$ mm) shows a tone at a frequency of 6.5 kHz, which again seems unrelated to the result obtained at $U_\infty = 26$ m/s. Regarding the amplitude, this case again is the one for which the lowest overall levels were calculated, while the highest amplitudes overall were obtained for the case with the thick cylinder and the small gap (case 6).

However, the strong sound pressure level fluctuations of the narrowband spectra as presented in Fig. 9, especially at medium and high frequencies, makes it hard to derive any clear trends. Thus, in a second step, all experimental results will be compared with the numerical ones in order to evaluate if the simulations can be used to obtain correct trends regarding the influence of the different parameters (cylinder diameter, length of the gap and flow speed) on the noise generation. This will be done for third-octave band spectra of the sound pressure level L_p . Fig. 10 shows this comparison for the lower flow speed of 26 m/s. Basically, it is visible that the experimental results show only minor

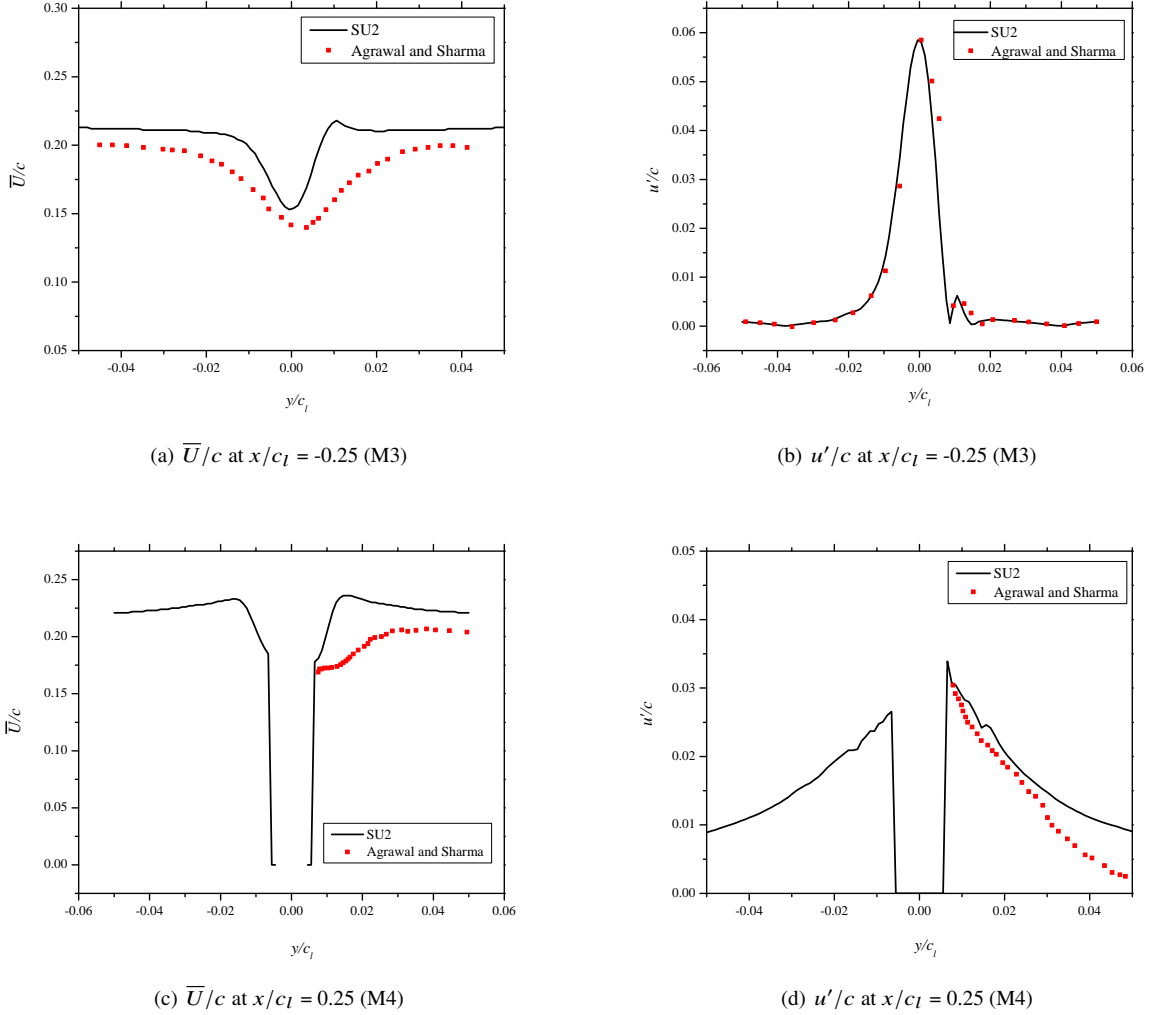


Fig. 8 Comparison of velocity profiles obtained at markers M3 and M4 (see Fig. 1) from the simulations with experimental data from [7]

differences (Fig. 10(a)). The cases with the 5 mm diameter cylinder show small peaks at a third-octave band center frequency of 1 kHz, which corresponds to the vortex shedding frequency of the cylinder and is assumed to be caused by the interaction of the vortex street with the airfoil leading edge. The cases with the thicker cylinder only show a maximum at a lower frequency band around 630 Hz, which is not due to the cylinder vortex shedding. The maximum caused by the cylinder vortex shedding would be expected around 340 Hz and hence below the lower frequency limit of the experimental setup. At frequencies roughly between 1 kHz and 4 kHz, the highest sound pressure levels are generated by the case with the 16 mm cylinder and the 124 mm gap, while at higher frequencies the noise generation for the case with the 16 mm cylinder and the 86 mm gap exceeds the noise from the other cases. The lowest levels are generated by the case with the 5 mm cylinder and the 124 mm gap. In general, the results from the calculations, shown in Fig. 10(b), do not agree well with the experimental results. Although the overall slope of the spectra is similar to the experimental results, the differences between the single cases are not reproduced, with the exception of the observation that the case with the 5 mm cylinder and the 124 mm gap generates the lowest sound pressure levels. The maxima due to the impingement of the von Kármán vortices are either not clearly distinguishable or are much higher than in the

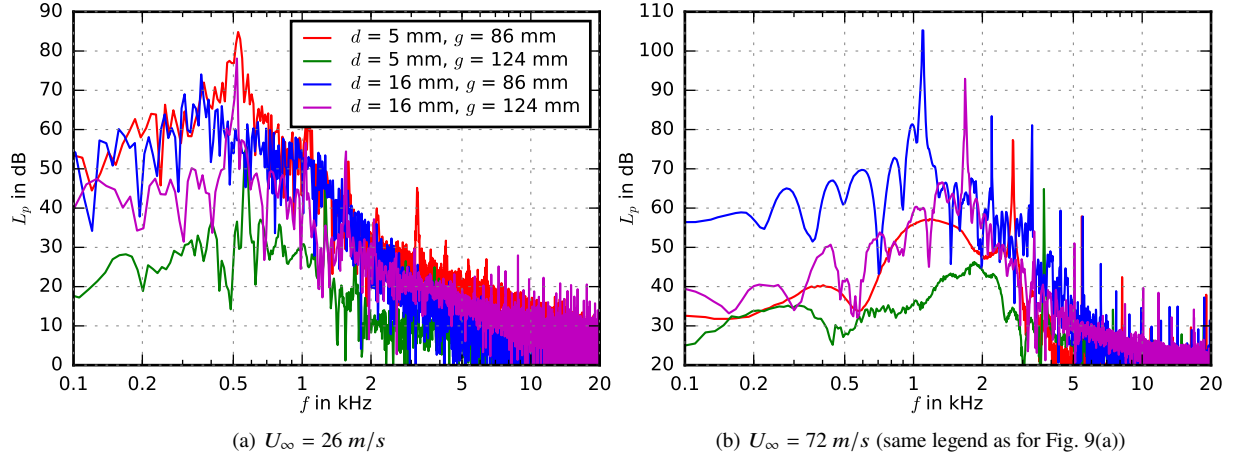


Fig. 9 Numerically obtained narrowband sound pressure level spectra for all cases (frequency step size 11.2 Hz)

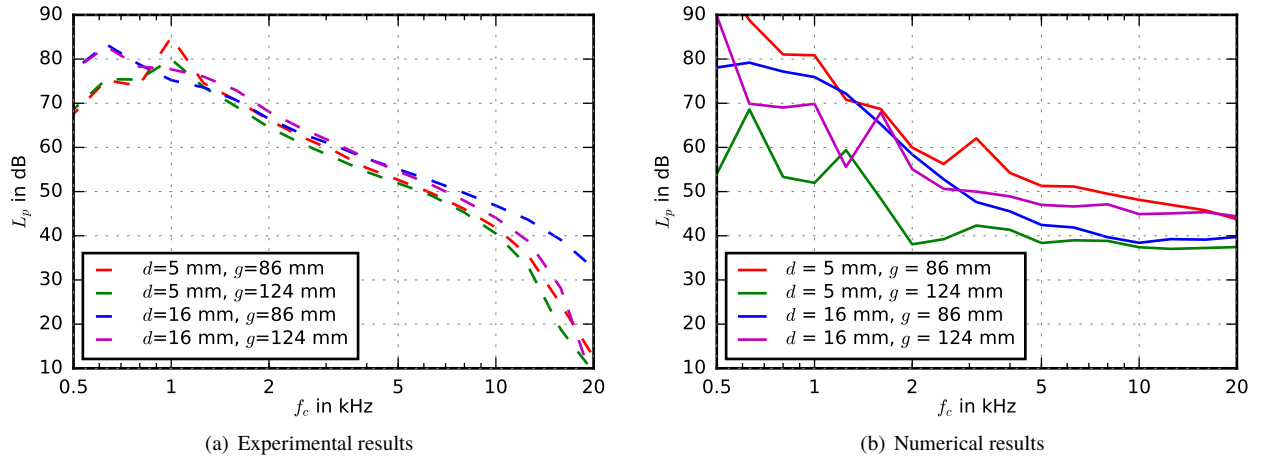


Fig. 10 Comparison of experimentally and numerically obtained third-octave band sound pressure level spectra for all cases at the lower flow speed of $U_\infty = 26 \text{ m/s}$

experimental cases.

The comparison between experimental results and numerical results for the higher flow speed of 72 m/s is then shown in Fig. 11. The experimental results (Fig. 11(a)) show a notable overall increase of the magnitude, which is due to the increase of the flow speed (airfoil leading edge noise can be assumed to be proportional to U^5 or U^6 , depending on the acoustic wavelength relative to the airfoil chord length [1]). The spectral maximum for the thicker cylinders remains at a frequency around 630 Hz, which is again not related to the cylinder vortex shedding. No distinct peak due to the interaction of the Kármán vortex street with the airfoil leading edge, which would be expected to appear around a frequency of 1 kHz, is visible in the spectra for the cases with the thick cylinders. At frequencies roughly between 800 Hz and 6.3 kHz, the noise from the case with the larger gap of 124 mm exceeds that from the case with the smaller gap, while at higher frequencies the opposite is true. For the thin cylinders, a maximum due to the interaction of the cylinder vortex street with the airfoil leading edge is visible in the 2.5 kHz third-octave band. For frequencies above this peak frequency, the sound pressure level is slightly higher for the case with the smaller gap, while at frequencies below the levels are practically the same. The results from the numerical simulations, shown in Fig. 11(b), again do not fully recover the experimental trends. However, several important observations are still possible. For example, maxima are

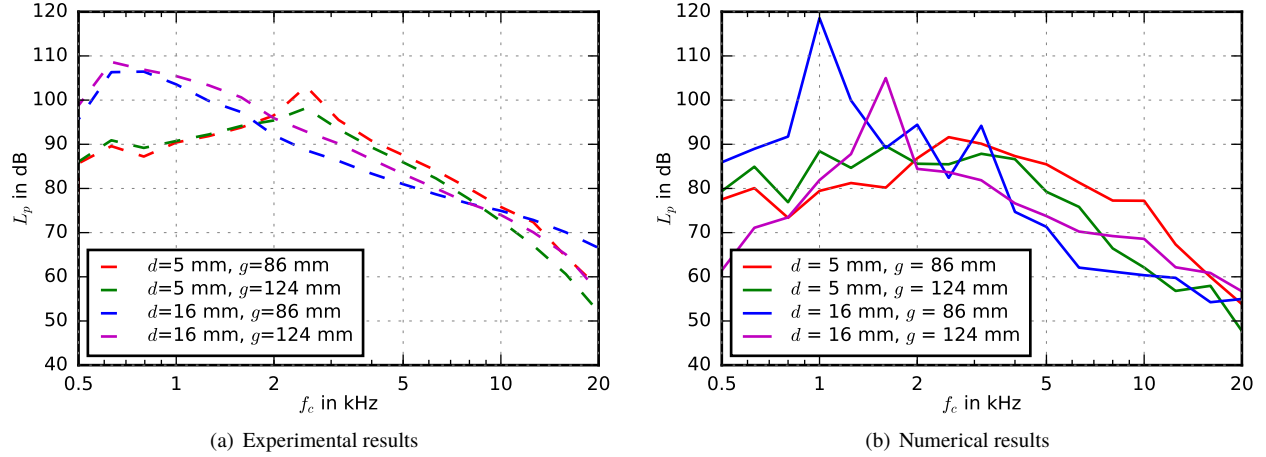


Fig. 11 Comparison of experimentally and numerically obtained third-octave band sound pressure level spectra for all cases at the higher flow speed of $U_\infty = 72$ m/s

predicted for the cases with the thick cylinder ($d = 16$ mm) at third-octave bands with center frequencies of 1 kHz (for the case with the 86 mm gap) and 1.6 kHz (for the case with the 124 mm gap). This corresponds to (or is close to) the theoretical value of 1 kHz obtained for a Strouhal number of 0.21 [28], although the experimental results did not contain corresponding peaks. For the cylinder with 5 mm diameter and a 86 mm gap, the predicted maximum can be seen at 2.5 kHz, which agrees with the experimental result for this case. It is difficult to observe a clear maximum for the thin cylinder and the larger gap of 124 mm due to the presence of several local maxima, but when taking the overall spectral shape into account, the maximum would be located roughly between 1.6 kHz and 2.5 kHz. Again, this agrees sufficiently with the experimental results. In agreement with the experiments, the simulations also reveal the trend that the noise generated by the case with the thin cylinder and the smaller gap exceeds that from the case with the thin cylinder and the larger gap at medium and high frequencies.

Overall, it seems that the 2D simulations are not capable to fully reproduce the correct trends observed in the experiments, but the agreement is generally better for the cases at higher flow speeds. In what follows, the results from the simulations will be compared to the experimental ones for every single case.

Fig. 12 shows the spectral analysis of the sound pressure level L_p for all cases that contain the thin cylinder with a diameter d of 5 mm. It can be observed that there is good agreement between simulation and measurement for the cases with the small gap of 86 mm (case 1, Fig. 12(a), and case 2, Fig. 12(b)), especially at frequencies above 4 kHz. For these cases, it seems that the simulation results match the experimental results even better at the lower flow speed of 26 m/s. Basically, the agreement is less good for the cases with the long gap of 124 mm (case 3, Fig. 12(c), and case 4, Fig. 12(d)), where the simulations notably underpredict the radiated sound pressure level (apart from a range of high frequencies above 10 kHz for case 3). This is especially true for the lower flow speed of 26 m/s (Fig. 12(c)), with differences between numerical and experimental results of more than 20 dB at low frequencies. A possible explanation for this trend is that the turbulence decays much faster in the simulations than in the experiments. Another possible reason is the relatively short simulation time of only 0.1 s: When observing the vorticity plots shown in Fig. 6 for a case with a smaller gap, it can be concluded that it takes already about 4500 iterations until the first eddies “hit” the airfoil leading edge at the lower flow speed of 26 m/s. Thus, if the gap width is increased to 124 mm, it can be assumed that it takes nearly half the simulation time until the eddies hit the leading edge.

The sound pressure level spectra for the cases with the thicker cylinder of 16 mm diameter are then shown in Fig. 13. In general, the agreement between simulation and experiment for most cases is comparable to that of the configurations with the small cylinder and the large gap, with differences of more than 10 dB. Again, a trend can be seen that the numerical results are lower than the experimental ones, except for a range of high frequencies in the cases with the lower flow speed (case 5 and case 7). This supports the thesis that, in general, the turbulence in the simulations decays faster than in the experiments.

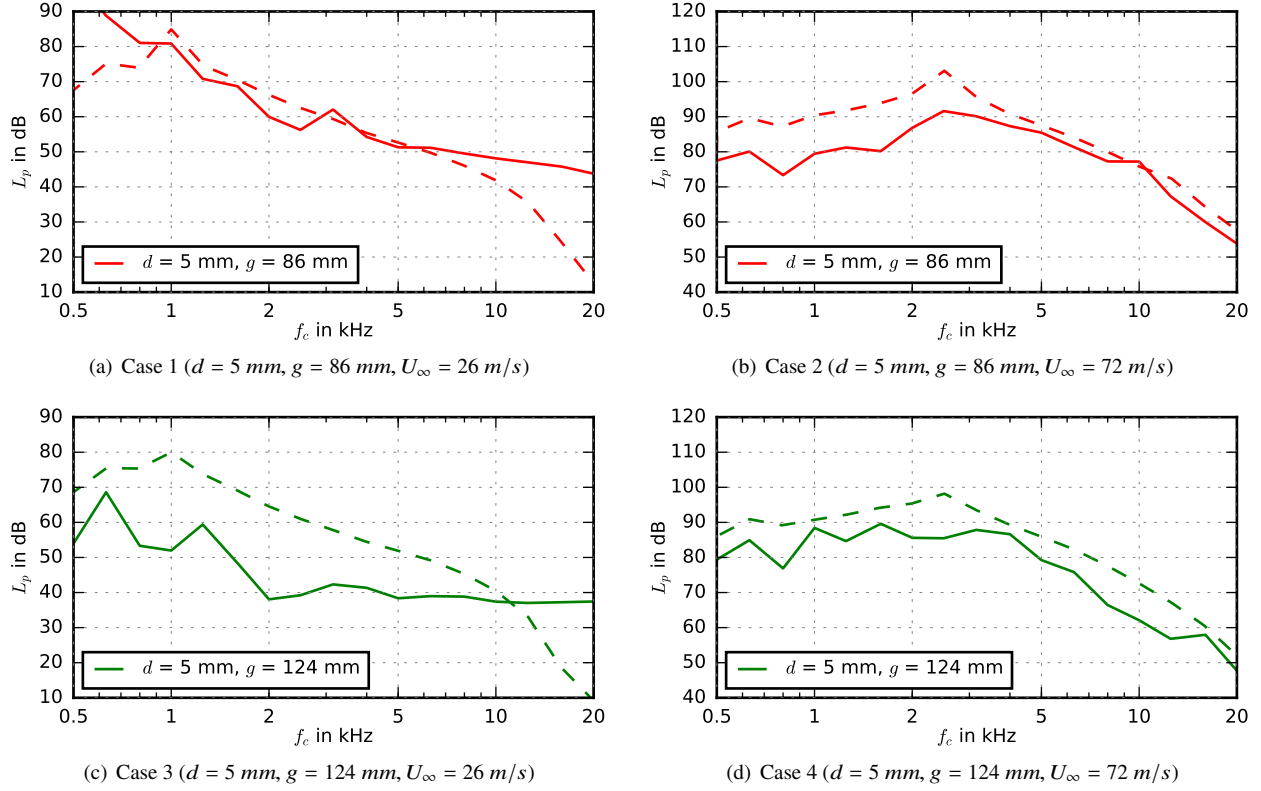


Fig. 12 Comparison of calculated (solid lines) and measured (dashed lines) third-octave band sound pressure level (L_p) for all cases involving the 5 mm cylinder

VI. Conclusion and Outlook

A numerical study on the noise generated by a rod-airfoil configuration was performed using the Detached-Eddy Simulation suite of the SU2 solver coupled with the Ffowcs-Williams and Hawkings technique. The results were compared to experimental results from a detailed wind tunnel study. The aim was to study the effect of variations of the configuration parameters (mainly the diameter of the cylinder, the distance between the rod and the leading edge of the airfoil and the flow speed) on the noise generation. Since the simulations were only two-dimensional, which is known to be problematic especially regarding the reproduction of the cylinder-generated turbulence, the main focus was to study whether the same trends could be observed in the simulations as were obtained from the experiments.

Basically, it was found that the simulated velocity profiles at different streamwise stations agreed sufficiently well with experimental data from Agrawal and Sharma [7]. However, regarding the noise generation, the study also showed that 2D simulations only enable a very basic prediction of the spectral shape and the trends observed in the experiments. In most cases, the simulated sound pressure levels are below the measured ones. Possible reasons for the deviations between the predicted acoustic results and the experimental ones is the relatively short simulation time as well as the constraint of a two-dimensional analysis.

In a future numerical study, 3D simulations will be performed for all tested configurations. Thus, it can be expected that the three-dimensional nature of the cylinder vortices will be better captured. As an example, Fig. 14 shows flow structures visualized by iso-surfaces of the Mach number-coloured Q-criterion for the case with a cylinder diameter of 10 mm and a gap of 86 mm at $U_\infty = 26$ m/s. The plot visualizes the three-dimensional nature of the vortices, thus underlining the benefit of 3D simulations.

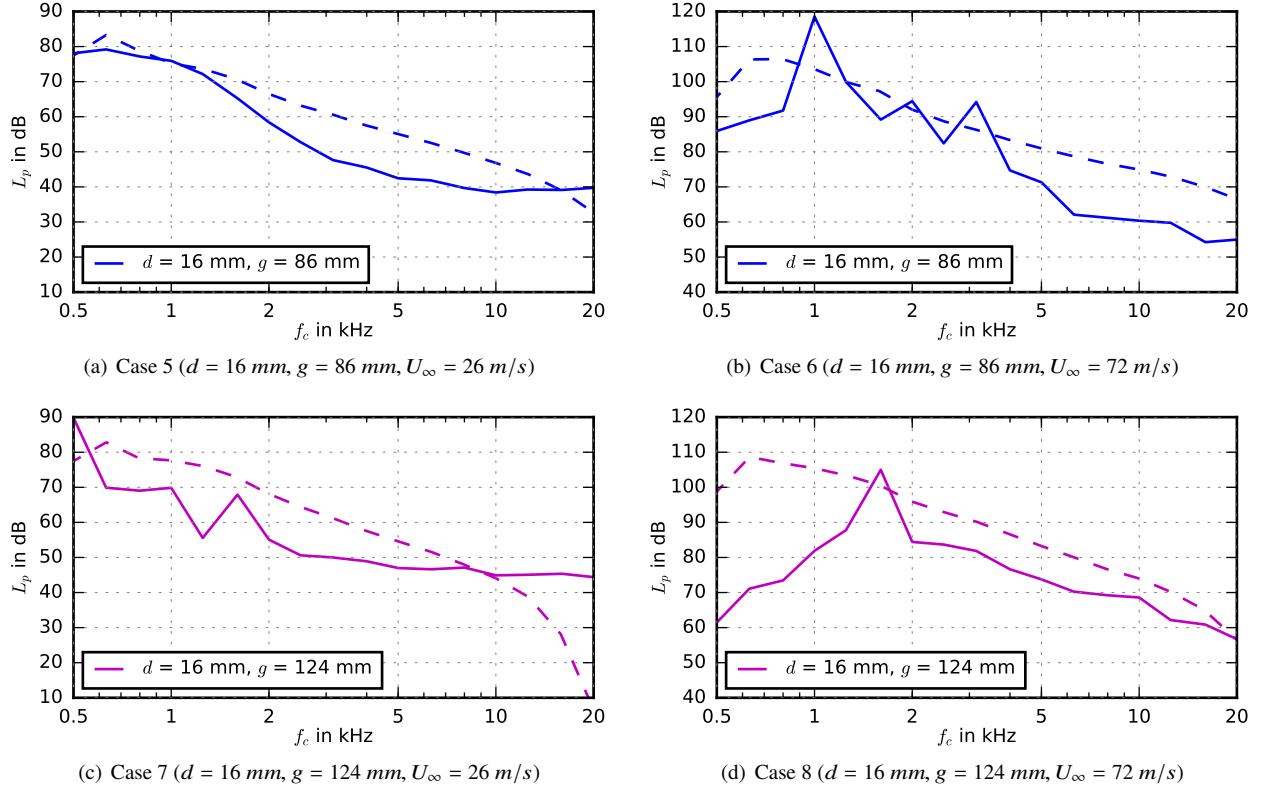


Fig. 13 Comparison of calculated (solid lines) and measured (dashed lines) third-octave band sound pressure level (L_p) for all cases involving the 16 mm cylinder

Acknowledgments

The authors take this opportunity to acknowledge the funding for this work, which was provided by the *Graduate Research School (GRS)* of BTU within the context of a Research Assistantship, and the additional funding provided by the *Center for Flow and Transport Modelling and Measurement (CFTM²)*. The participation at the 25th AIAA/CEAS Aeroacoustics Conference 2019 was financially supported by the *Deutsche Gesellschaft für Akustik (DEGA)* within the framework of a Young Scientist Grant, which is gratefully acknowledged.

We are also thankful to Dr. Jens Giesler for his experimental data, which he obtained during his doctoral studies at BTU, to Dr. Beckett Y. Zhou (Technical University Kaiserslautern) for the valuable discussions and to Erik W. Schneehagen for his help with the setup of the 3D simulation.

References

- [1] Blake, W., *Mechanics of Flow-Induced Sound and Vibration, Volume II: Complex Flow-Structure Interactions*, Academic Press, Inc., 1986.
- [2] Zdravkovich, M. M., *Flow around circular cylinders: A comprehensive guide through flow phenomena, experiments, applications, mathematical models, and computer simulations*, Oxford University Press, 1997.
- [3] Casalino, D., Jacob, M., and Roger, M., "Prediction of Rod-Airfoil Interaction Noise Using the Ffowcs-Williams-Hawkings Analogy," *AIAA Journal*, Vol. 41, No. 2, 2003, pp. 182–191. doi:10.2514/2.1959.
- [4] Jacob, M. C., Boudet, J., Casalino, D., and Michard, M., "A rod-airfoil experiment as a benchmark for broadband noise modeling," *Theoretical and Computational Fluid Dynamics*, Vol. 19, No. 3, 2005, pp. 171–196. doi:10.1007/s00162-004-0108-6.

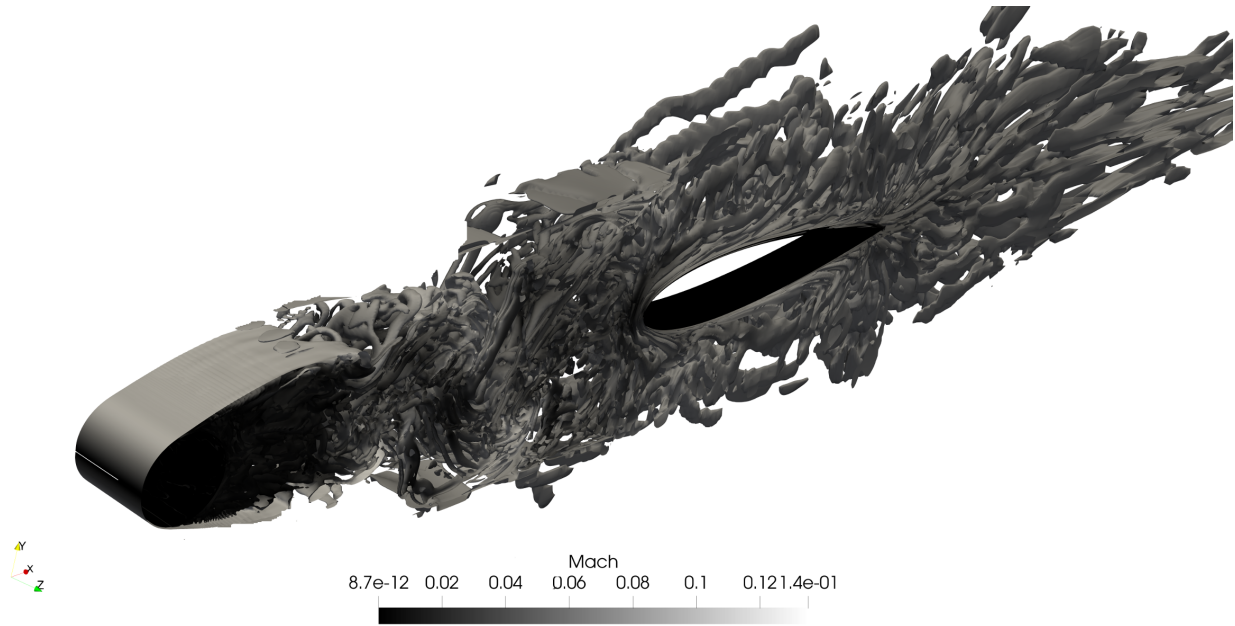


Fig. 14 Example result of a 3D simulation (shown is the flow structures visualized by iso-surfaces of Mach number-coloured Q-criterion for the case with a cylinder diameter of 10 mm and a gap of 86 mm at $U_\infty = 26$ m/s)

- [5] Berland, J., Lafon, P., Crouzet, F., and Daude, F., “Numerical Insight into Sound Sources of a Rod-Airfoil Flow Configuration Using Direct Noise Calculation,” *16th AIAA/CEAS Aeroacoustics Conference*, ????
- [6] Giret, J.-C., Sengissen, A., Moreau, S., Sanjosé, M., and Jouhaud, J.-c., “Prediction of the sound generated by a rod-airfoil configuration using a compressible unstructured LES solver and a FW-H analogy,” *18th AIAA/CEAS Aeroacoustics Conference (33rd AIAA Aeroacoustics Conference)*, AIAA paper 2012-2058, 2012.
- [7] Agrawal, B. R., and Sharma, A., “Numerical analysis of aerodynamic noise mitigation via leading edge serrations for a rod–airfoil configuration,” *International Journal of Aeroacoustics*, Vol. 15, No. 8, 2016, pp. 734–756.
- [8] Jiang, Y., Mao, M. L., Deng, X. G., and Liu, H. Y., “Numerical investigation on body-wake flow interaction over rod-airfoil configuration,” *Journal of Fluid Mechanics*, Vol. 779, 2015, pp. 1–35. doi:10.1017/jfm.2015.419.
- [9] Jiang, M., Li, X.-d., and Zhou, J.-j., “Experimental and numerical investigation on sound generation from airfoil-flow interaction,” *Applied Mathematics and Mechanics*, Vol. 32, No. 6, 2011, pp. 765–776. doi:10.1007/s10483-011-1456-7.
- [10] Geyer, T. F., Sharma, S., and Sarradj, E., “Detached Eddy Simulation of the Flow Noise Generation of Cylinders with Porous Cover,” *2018 AIAA/CEAS Aeroacoustics Conference*, AIAA paper 2018-3472, 2018.
- [11] Greschner, B., Thiele, F., Casalino, D., and Jacob, M., “Influence of Turbulence Modeling on the Broadband Noise Simulation for Complex Flows,” *10th AIAA/CEAS Aeroacoustics Conference*, AIAA paper 2010-3705, ???
- [12] Zhou, B., Albring, T. A., Gauger, N. R., Ilario, C., Economon, T. D., and Alonso, J. J., “Reduction of Airframe Noise Components Using a Discrete Adjoint Approach,” *18th AIAA/ISSMO Multidisciplinary Analysis and Optimization Conference*, AIAA paper 2017-3658, 2017.
- [13] Ffowcs Williams, J. E., and Hawkings, D. L., “Sound Generation by Turbulence and Surfaces in Arbitrary Motion,” *Philosophical Transactions of the Royal Society A: Mathematical, Physical and Engineering Sciences*, Vol. 264, No. 1151, 1969, pp. 321–342. doi:10.1098/rsta.1969.0031.
- [14] Giesler, J., and Sarradj, E., “Measurement of broadband noise generation on rod-airfoil-configurations,” *15th AIAA/CEAS Aeroacoustics Conference (30th AIAA Aeroacoustics Conference)*, AIAA paper 2009-3308, 2009.

- [15] Giesler, J., “Schallentstehung durch turbulente Zuströmung an aerodynamischen Profilen,” Doctoral thesis, Brandenburg University of Technology, Cottbus, 2011.
- [16] Galdeano, S., Barré, S., and Réau, N., “Noise radiated by a rod-airfoil configuration using DES and the Ffowcs-Williams & Hawkings’ analogy,” *16th AIAA/CEAS Aeroacoustics Conference, AIAA paper 2010-3702*, 2010.
- [17] Greschner, B., Thiele, F., Jacob, M. C., and Casalino, D., “Prediction of sound generated by a rod–airfoil configuration using EASM DES and the generalised Lighthill/FW-H analogy,” *Computers & Fluids*, Vol. 37, No. 4, 2008, pp. 402–413. doi:10.1016/j.compfluid.2007.02.013.
- [18] Caraeni, M., Dai, Y., and Caraeni, D., “Acoustic Investigation of Rod Airfoil Configuration with DES and FWH,” *37th AIAA Fluid Dynamics Conference and Exhibit, AIAA paper 2007-4106*, 2007.
- [19] Gerolymos, G. A., and Vallet, I., “Influence of Temporal Integration and Spatial Discretization on Hybrid RSM-VLES Computations,” *18th AIAA Computational Fluid Dynamics Conference, AIAA paper 2007-4094*, 2007.
- [20] Economon, T. D., Palacios, F., Copeland, S. R., Lukaczyk, T. W., and Alonso, J. J., “SU2: An open-source suite for multiphysics simulation and design,” *Aiaa Journal*, Vol. 54, No. 3, 2015, pp. 828–846.
- [21] Molina, E., Spode, C., Annes da Silva, R. G., Manosalvas-Kjono, D. E., Nimmagadda, S., Economon, T. D., Alonso, J. J., and Righi, M., “Hybrid rans/les calculations in su2,” *23rd AIAA Computational Fluid Dynamics Conference, AIAA paper 2017-4284*, 2017.
- [22] Molina, E., Zhou, B. Y., Alonso, J. J., Righi, M., and Silva, R. G., “Flow and Noise Predictions Around Tandem Cylinders using DDES approach with SU2,” *AIAA Scitech 2019 Forum, AIAA paper 2019-0326*, 2019.
- [23] Sarradj, E., Fritzsche, C., Geyer, T., and Giesler, J., “Acoustic and aerodynamic design and characterization of a small-scale aeroacoustic wind tunnel,” *Applied Acoustics*, Vol. 70, No. 8, 2009, pp. 1073–1080. doi:10.1016/J.APACOUST.2009.02.009.
- [24] Sarradj, E., and Herold, G., “A Python framework for microphone array data processing,” *Applied Acoustics*, Vol. 116, 2017, pp. 50–58.
- [25] Brooks, T. F., and Humphreys, W. M., “A deconvolution approach for the mapping of acoustic sources (DAMAS) determined from phased microphone arrays,” *Journal of Sound and Vibration*, Vol. 294, No. 4-5, 2006, pp. 856–879. doi:10.1016/J.JSV.2005.12.046.
- [26] Herold, G., and Sarradj, E., “Performance analysis of microphone array methods,” *Journal of Sound and Vibration*, Vol. 401, 2017, pp. 152–168.
- [27] Merino-Martinez, R., Sijtsma, P., Snellen, M., Ahlefeld, T., Antoni, J., Bahr, C. J., Blacodon, D., Ernst, D., Finez, A., Funke, S., Geyer, T. F., Haxter, S., Herold, G., Huang, X., Humphreys, W. M., Leclère, Q., Malgoezar, A., Michel, U., Padois, T., Pereira, A., Picard, C., Sarradj, E., Siller, H., Simons, D. G., and Spehr, C., “A review of acoustic imaging methods using phased microphone arrays,” *CEAS Aeronautical Journal*, 2019, pp. 1–34.
- [28] Schlichting, H., and Gersten, K., *Boundary-layer theory*, 9th edition, Springer, 1997.